Electronic Supplementary Material (ESI) for EES Catalysis.

Supplementary Information

An unexplored role of the CrO_x shell in an elaborated Rh/CrO_x core–shell cocatalyst for photocatalytic water splitting: a selective electron transport pathway from semiconductors to core metals, boosting charge separation and H_2 evolution

Tetsu Kotani, [‡a] Kanta Ogawa, [‡a†] Hajime Suzuki,[a] Kosaku Kato,[b] Osamu Tomita,[a] Akira Yamakata,[b] Ryu Abe[a]*

[a] Department of Energy and Hydrocarbon Chemistry, Graduate School of Engineering, Kyoto University, Nishikyo-ku, Kyoto 615-8510, Japan

[b] Graduate School of Natural Science and Technology, Okayama University, 3-1-1 Tsushima-naka, Kita-ku, Okayama 700-8530, Japan

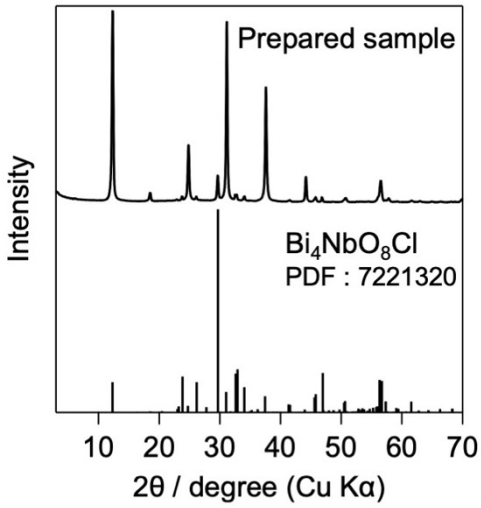

Figure S1. XRD pattern of Bi_4NbO_8Cl prepared via the flux method.

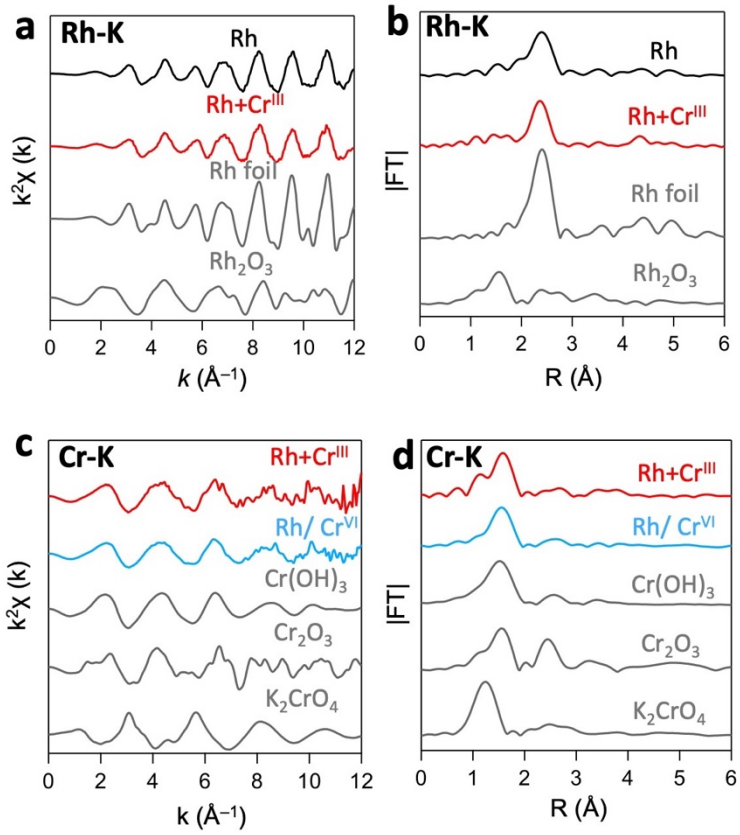

Figure S2. Rh K-edge (a) k^2-weighted EXAF and (b) Fourier transform of Rh, $Rh+Cr^{III}$ samples along with Rh foil and Rh_2O_3 as references. Cr K-edge (c) k^2-weighted EXAF and (d) Fourier transform of $Rh+Cr^{III}$, Rh/Cr^{VI} samples along with $Cr(OH)_3$, Cr_2O_3, K_2CrO_4 as references.

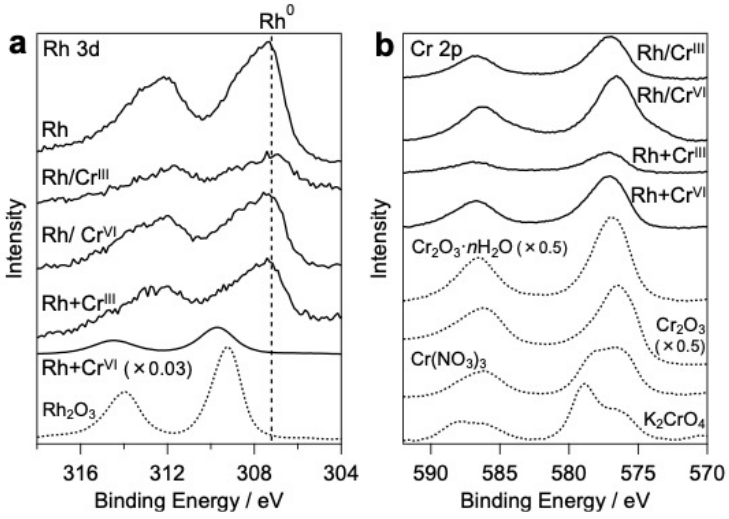

Figure S3. Rh 3d and Cr 2p XPS results of Rh and Cr - loaded Bi_4NbO_8Cl prepared via stepwise (Rh/Cr^{III}, Rh/Cr^{VI}) and simultaneous deposition ($Rh+Cr^{III}$, $Rh+Cr^{VI}$). The Rh 3d spectrum of Rh_2O_3 and the Cr 2p spectra of Cr_2O_3, $Cr(NO_3)_3$, and K_2CrO_4 are shown as references.

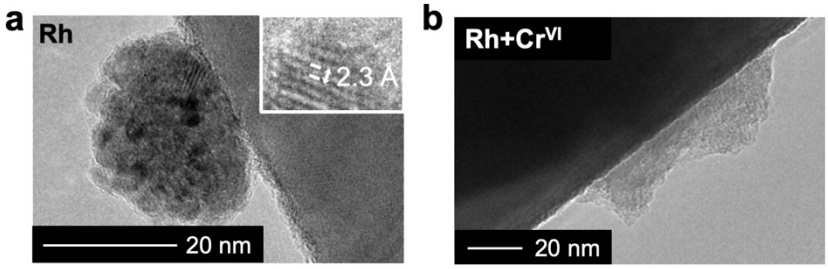

Figure S4. HR-TEM images of (a) Rh, (b) $Rh+Cr^{VI}$ loaded on Bi_4NbO_8Cl.

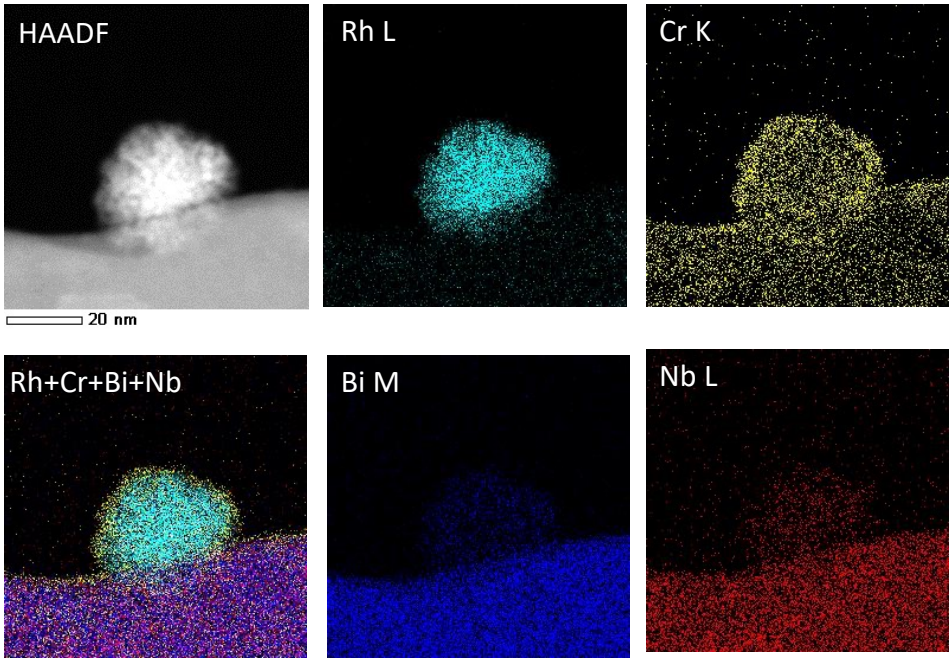

Figure S5. HAADS-STEM and EDX elemental mapping images of Rh/Cr^{III} sample.

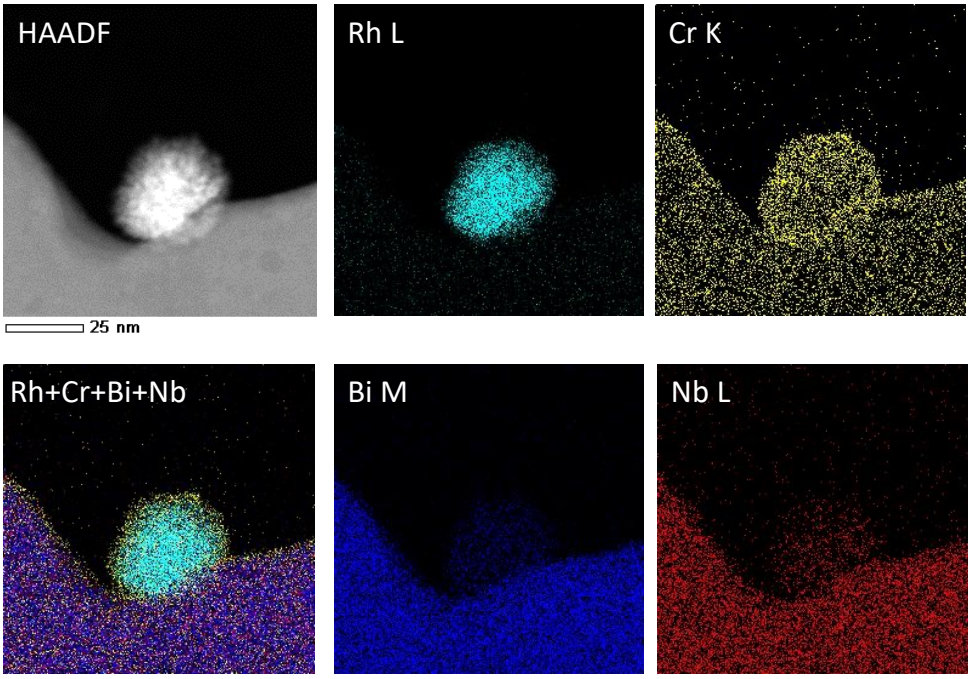

Figure S6. HAADS-STEM and EDX elemental mapping images of Rh/Cr^{VI} sample.

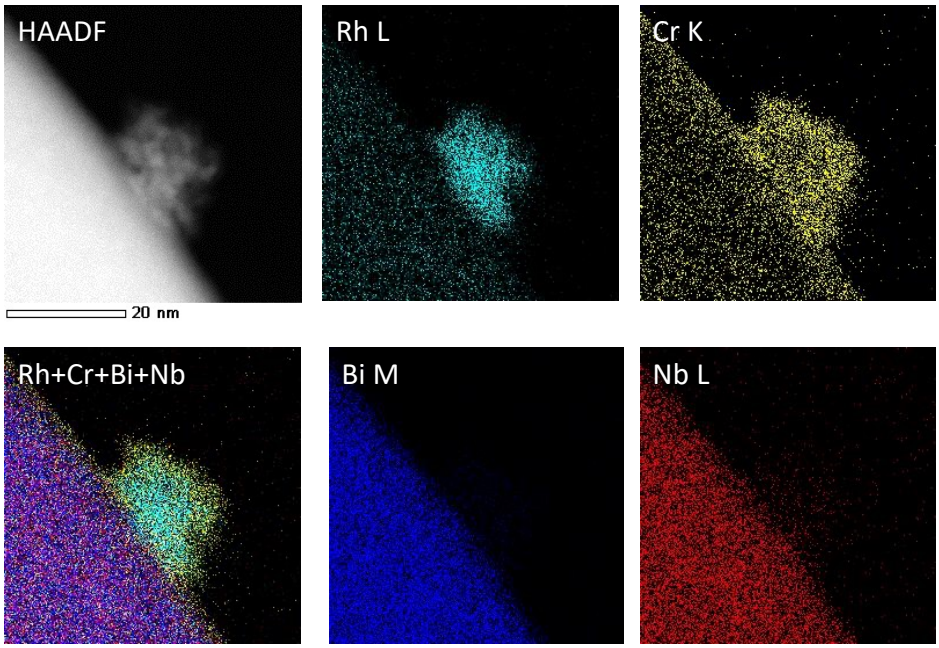

Figure S7. HAADS-STEM and EDX elemental mapping images of Rh+Cr^{III} sample.

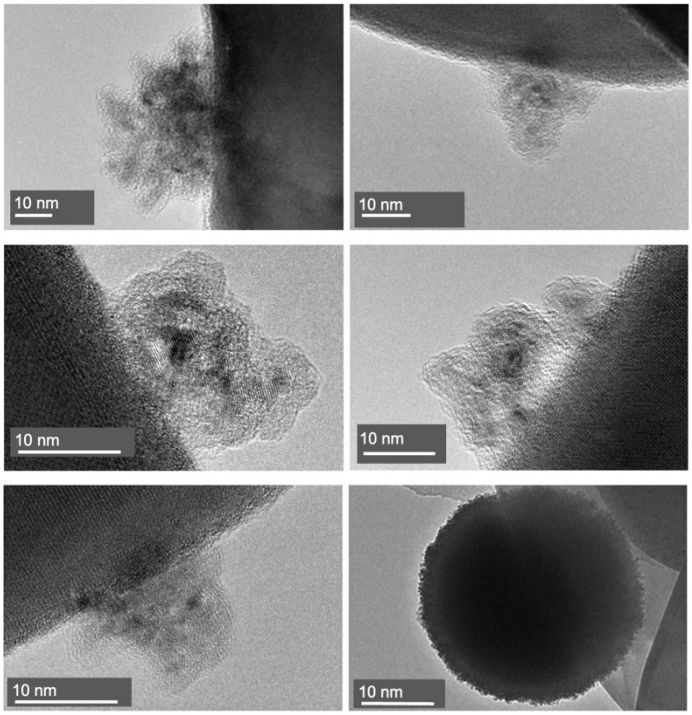

Figure S8. TEM images of Rh+Cr^{III} loaded Bi_4NbO_8Cl.

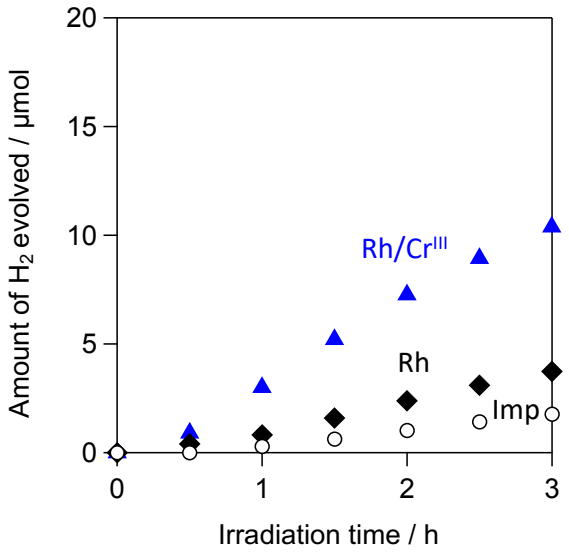

Figure S9. Time courses of H_2 evolution of Rh (black), Rh/Cr^{III} (blue), and Imp samples in an aqueous methanol solution (20 vol%, 250 mL) under visible light irradiation (λ > 400 nm). For Imp sample, CrO_x was deposited on the photocatalyst by the impregnation method using $Cr(NO_3)_3$ as a precursor under an Ar flow at 150 °C.

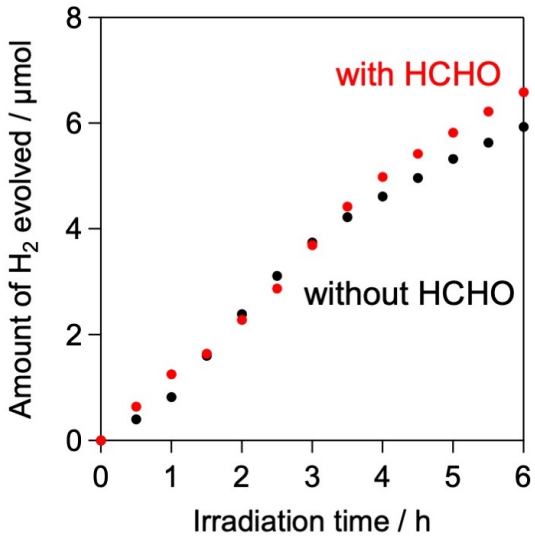

Figure S10. Time courses of H_2 evolution of Rh loaded samples in an aqueous methanol solution (20 vol%, 250 mL) with or without formaldehyde (HCHO).

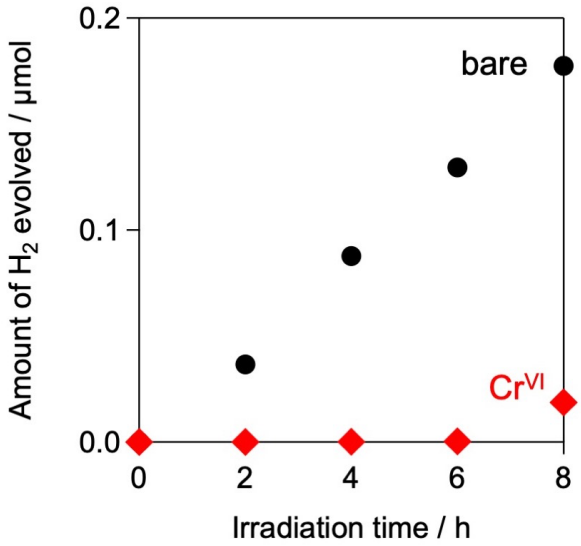

Figure S11. Time courses of H_2 evolution of bare or CrO_x-loaded Bi_4NbO_8Cl in an aqueous methanol

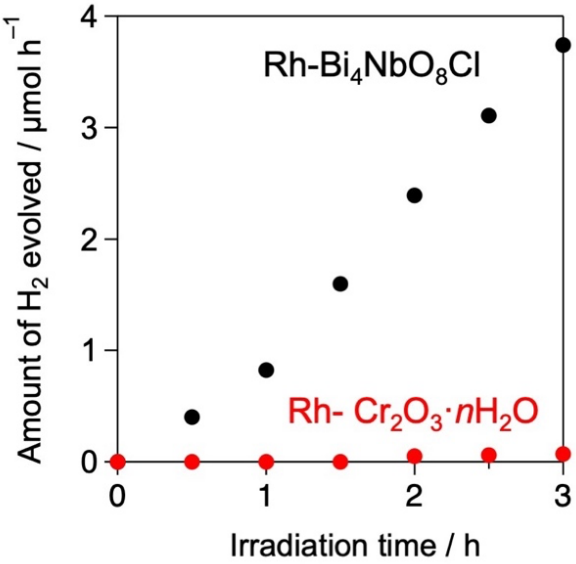

Figure S12. Time courses of H_2 evolution of Rh loaded Bi_4NbO_8Cl and Cr_2O_3•nH_2O samples in an aqueous methanol solution (20 vol%, 250 mL) under visible light ($\lambda > 400$ nm).

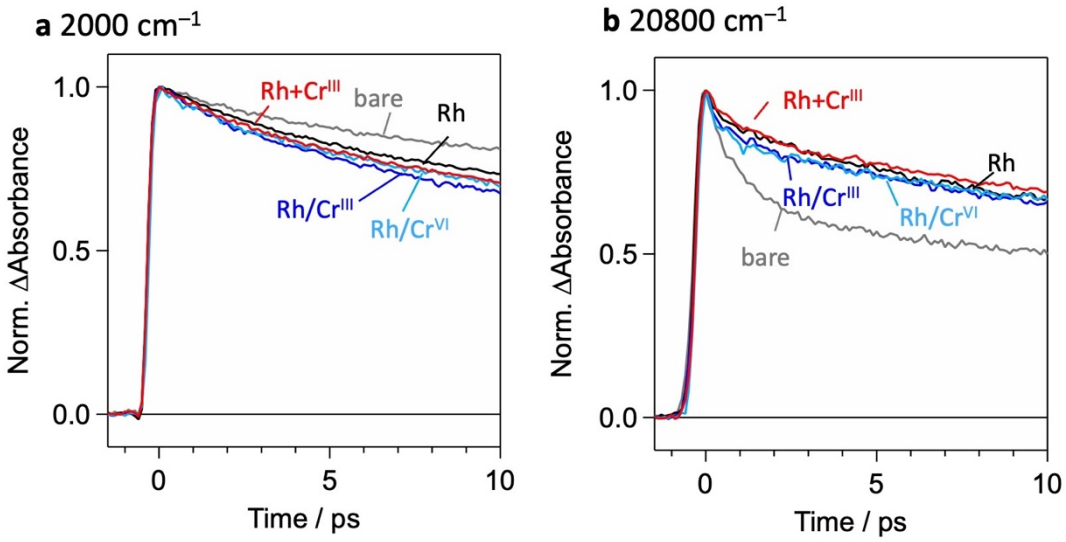

Figure S13. Femtosecond decay profiles of transient absorptions at (a) 2,000 cm^{-1} (b) and 20,800 cm^{-1}. The samples were excited by 355 nm laser pulses (90 fs duration, 6 μJ, 500 Hz) in in N_2 (20 Torr) for the several pico-second (ps) region.

Table S1. Fitting parameters for TA decays at 2,000 cm^{-1}. TA decays were fitted with single exponential function.

	A	*τ* / ps
bare	0.975 ± 0.02	50.5 ± 0.8
Rh	0.973 ± 0.02	33.6 ± 0.5
Rh/Cr^{VI}	0.963 ± 0.03	31.1 ± 0.4
Rh/Cr^{III}	0.961 ± 0.03	27.1 ± 0.4
$Rh+Cr^{III}$	0.955 ± 0.03	30.9 ± 0.5

Table S2. Fitting parameters for TA decays at 20,800 cm^{-1}. TA decays were fitted with single exponential function.

	A	*τ* / ps
bare	0.77 ± 0.01	20 ± 1
Rh	0.901 ± 0.004	30.0 ± 0.6
Rh/Cr^{VI}	0.866 ± 0.004	36 ± 2
Rh/Cr^{III}	0.882 ± 0.004	31.1 ± 0.9
$Rh+Cr^{III}$	0.911 ± 0.004	33.9 ± 0.5

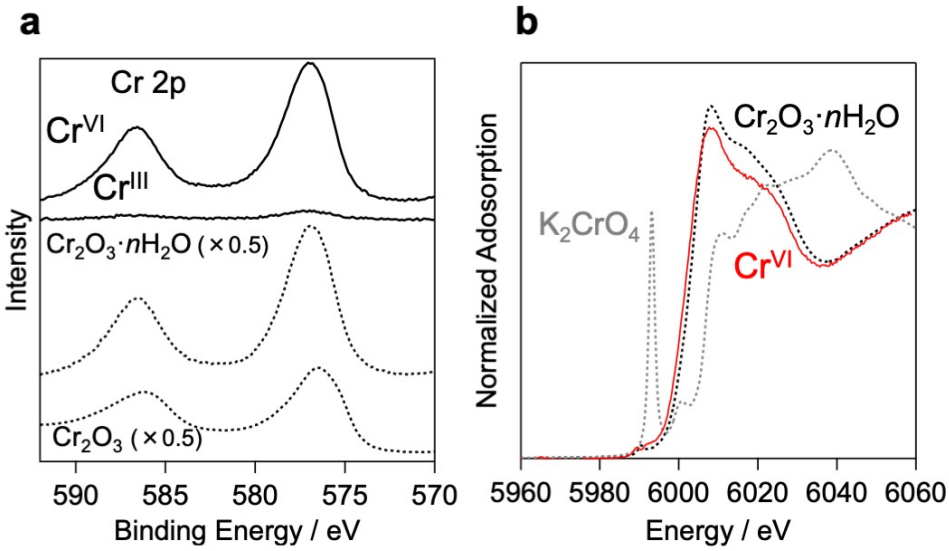

Figure S14 (a) Cr 2p X-ray photoelectron and Cr-K edge XANES spectra of the sample after photoirradiation in a methanol solution containing K_2CrO_4 or $Cr(NO_3)_3$ solution under visible light (λ > 400 nm).

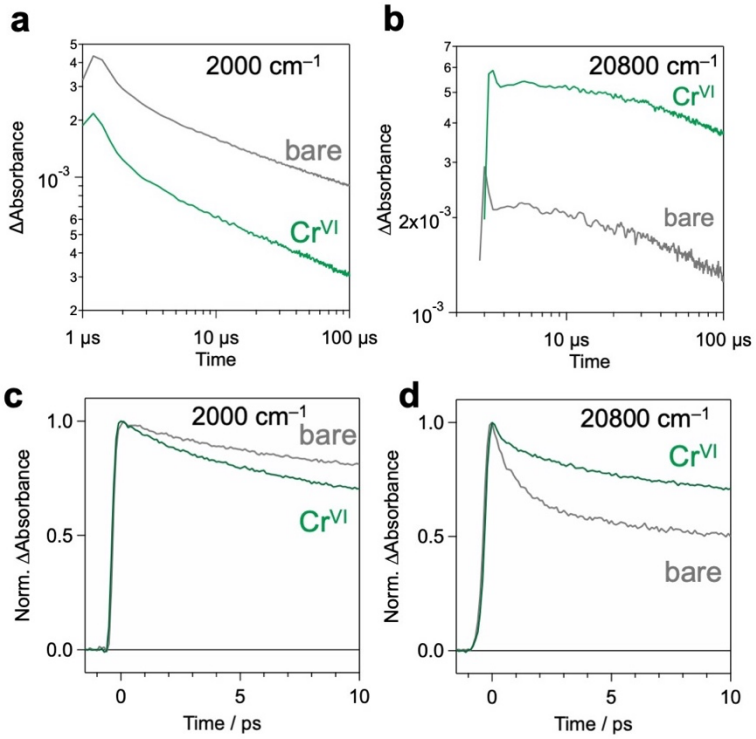

Figure S15. Decay kinetics of TA in the (a, b) microsecond and (c, d) picosecond regions measured at (a, c) 2000 cm^{-1} and (b, d) 20800 cm^{-1} in N_2 (20 Torr). The samples were excited by UV laser pulses (355 nm, 0.5 mJ cm^{-2}). The CrO_x-loaded Bi_4NbO_8Cl sample was prepared via photodeposition of $K_2Cr^{VI}O_4$, providing almost same valence state of Cr as those in Rh/Cr^{III}, Rh/Cr^{VI}, and $Rh+Cr^{III}$ (i.e., $Cr_2O_3•nH_2O$, see Figure S14). The CrO_x loading on Bi_4NbO_8Cl surface significantly decreases the IR signal but increases the visible signal in the microsecond region, while the initial decay process could not be observed due to the limit of the time resolution. The carrier transfer from semiconductors to cocatalysts generally takes place on the pico-to-nanosecond time scale.[8,26,31] Indeed, the TA measurements in picosecond region (c, d) clearly show the initial process, in which the CrO_x loading accelerated the decay of the electron (IR) but deaccelerated that of holes (visible).

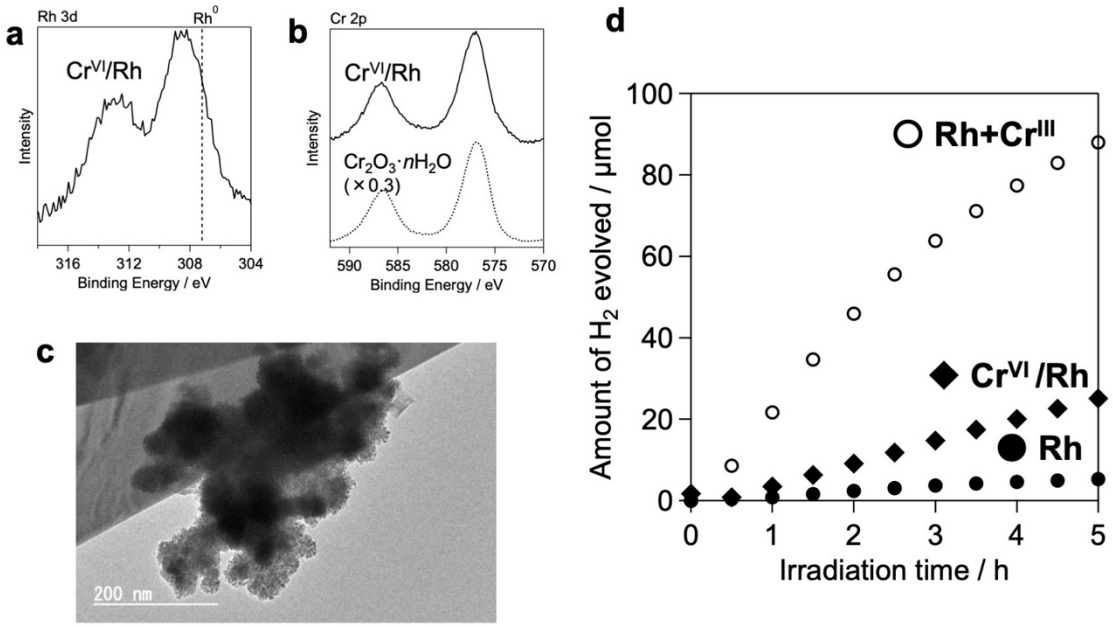

Figure S16. (a) Rh 3d and (b) Cr 2p X-ray photoelectron spectra, and (c) TEM images of a sample loaded with CrO_x prior to Rh. The spectra of reference samples are shown as dotted lines. (d) Time courses of H_2 evolution of a sample loaded with CrO_x prior to Rh (Cr^{VI}/Rh). The CrO_x was deposited on Bi_4NbO_8Cl via the photoreduction of Cr^{VI} species.

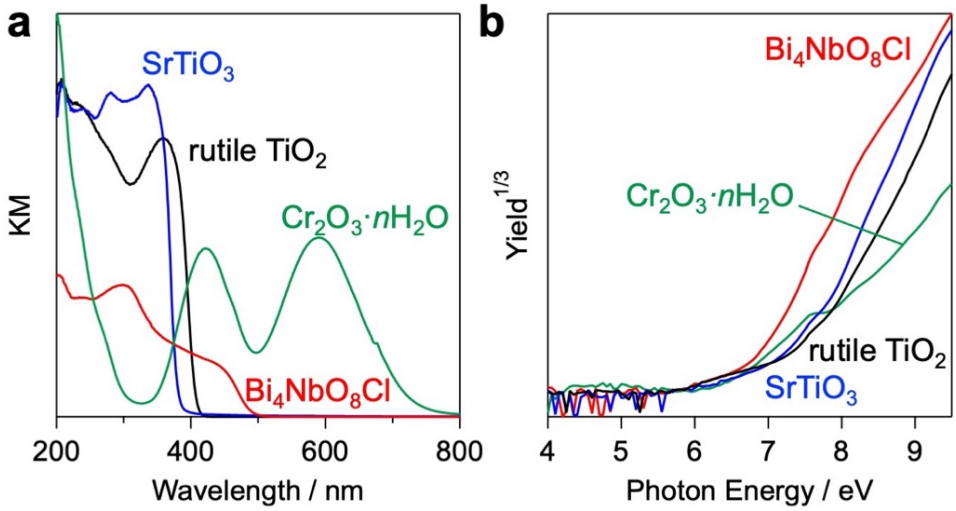

Figure S17. (a) Diffuse reflection spectra and (b) photoemission yield spectra of Bi_4NbO_8Cl, $Cr_2O_3 \cdot nH_2O$, $SrTiO_3$, and TiO_2.

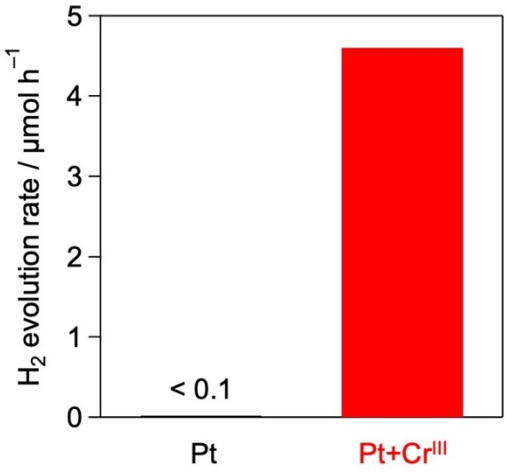

Figure S18. Rates of H_2 evolution over Pt and Pt+Cr^{III} loaded Bi_4NbO_8Cl samples. The reactions were conducted in an aqueous methanol solution (20 vol%, 250 mL) under visible light irradiation ($\lambda > 400$ nm).

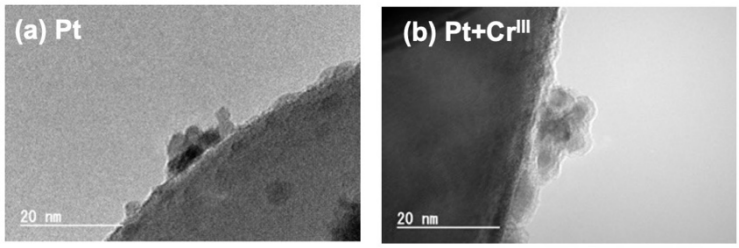

Figure S19. TEM images of (a) Pt, (b) Pt+Cr^{III} loaded Bi_4NbO_8Cl.

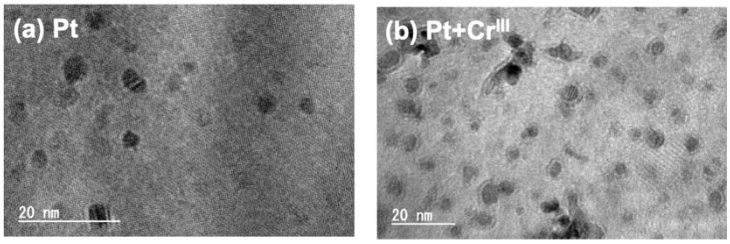

Figure S20. TEM images of (a) Pt, (b) Pt+Cr^{III} loaded on the dominant facet ((001)) of Bi_4NbO_8Cl.

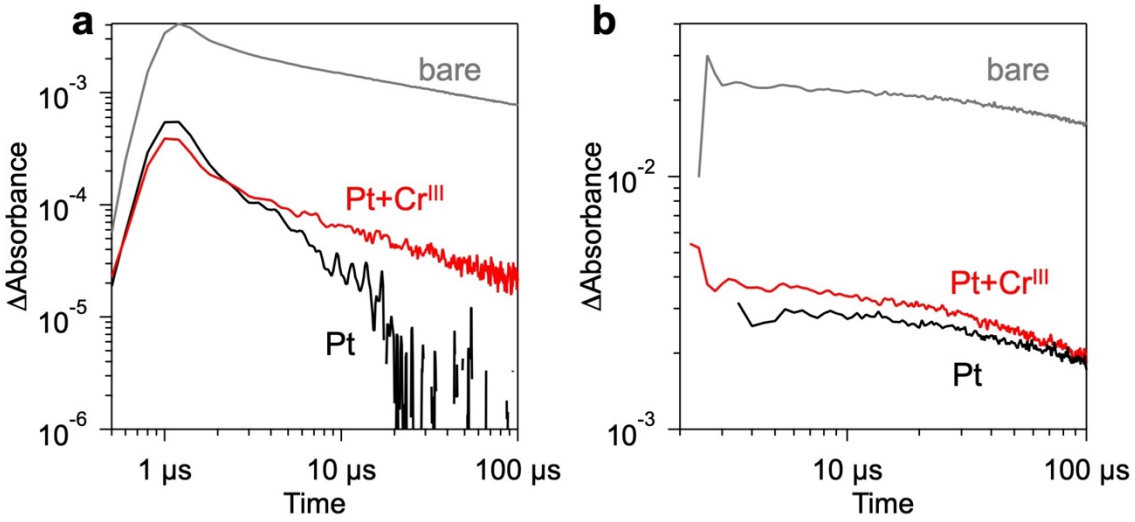

Figure S21. TA decay kinetics of bare (gray), Pt (black), and Pt+Cr^{III} (red) samples in microsecond regions measured at (a) 2000 cm^{-1} and (b) 20800 cm^{-1} in N_2 (20 Torr). The samples were excited by UV laser pulses (355 nm).

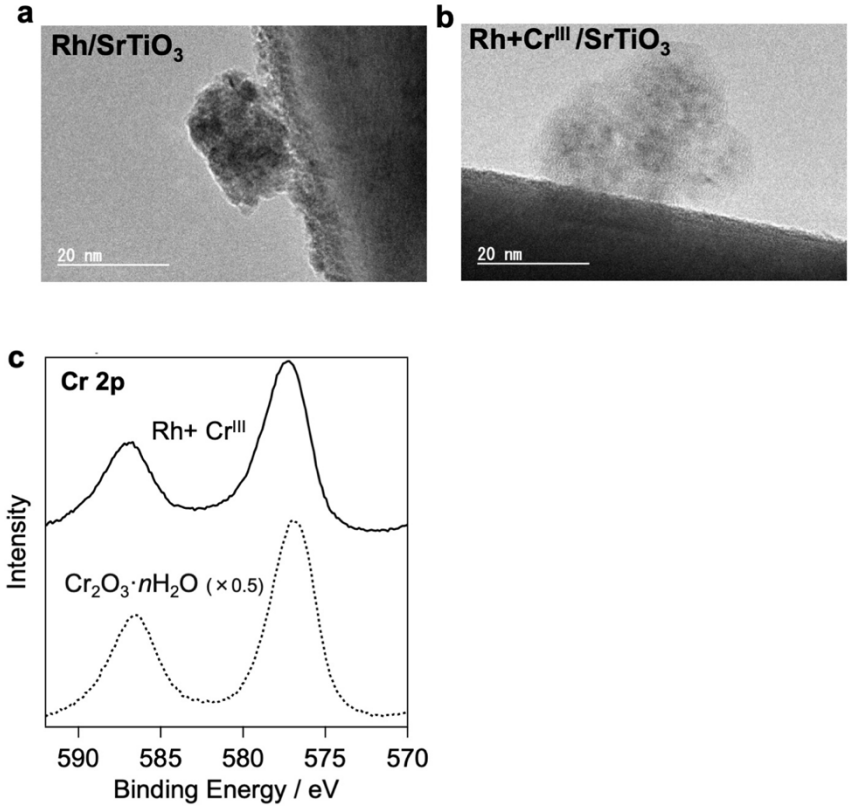

Figure S22. TEM images of (a) Rh, (b) Rh+Cr^{III}/$SrTiO_3$. c, XPS spectra for Rh+Cr^{III}/$SrTiO_3$ focusing on the Cr 2p region.

Table S3. H_2 evolution rates of various semiconductor photocatalysts loaded with Rh or Rh+Cr^{III}. In the case if Bi_4NbO_8Cl, Rh+Cr^{III} shows a 30 times higher activity than Rh, while for $SrTiO_3$ the improvement rate is only double, which suggests that the effect of CrO_x loading on the activity is smaller in $SrTiO_3$ than in Bi_4NbO_8Cl. Due to the smaller effect of CrO_x on the activity of $SrTiO_3$, other factor may contribute to the activity. For example, Rh in Rh+Cr^{III} is not fully reduced (Figure S23), which may cause the lower activity of Rh+Cr^{III} than Rh/Cr^{VI} in the case of $SrTiO_3$.

		Rh	Rh/Cr^{VI}	Rh+Cr^{III}
Bi_4NbO_8Cl	λ > 400 nm	0.82	3.18	24.28
$SrTiO_3$	λ > 300 nm	25.0	69.5	53.2
rutile TiO_2	λ > 300 nm	156.7	1.48	27.7

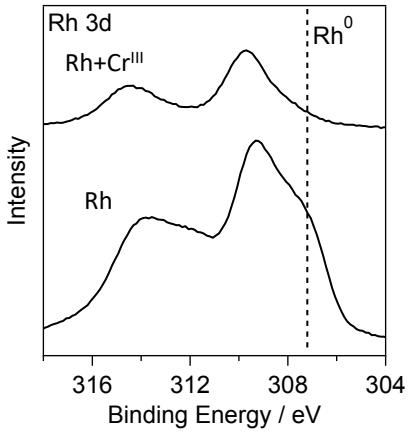

Figure S23. Rh 3d X-ray photoelectron spectra of Rh and Rh+Cr^{III} loaded $SrTiO_3$.

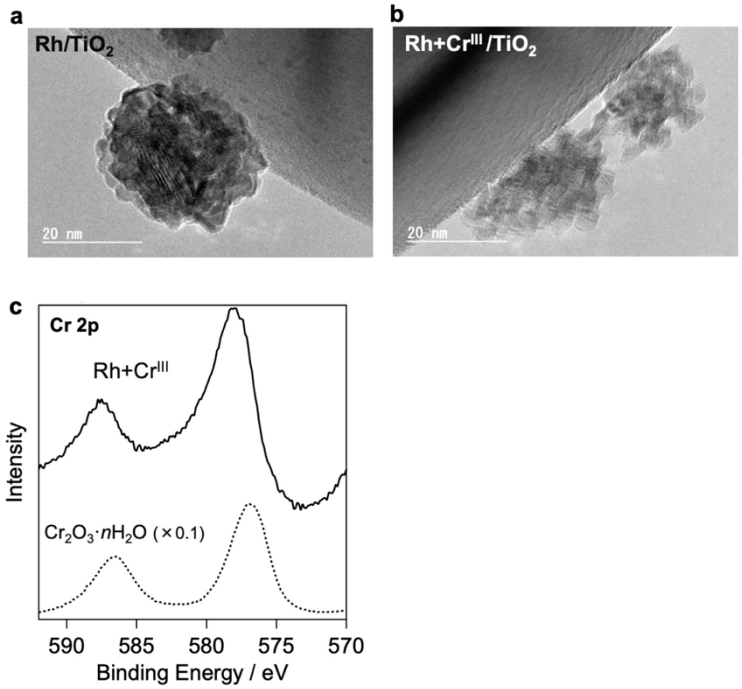

Figure S24. TEM images of (a) Rh, (b) Rh+Cr^{III}/TiO_2. c, XPS spectra for Rh+Cr^{III}/TiO_2 focusing on the Cr 2p region.

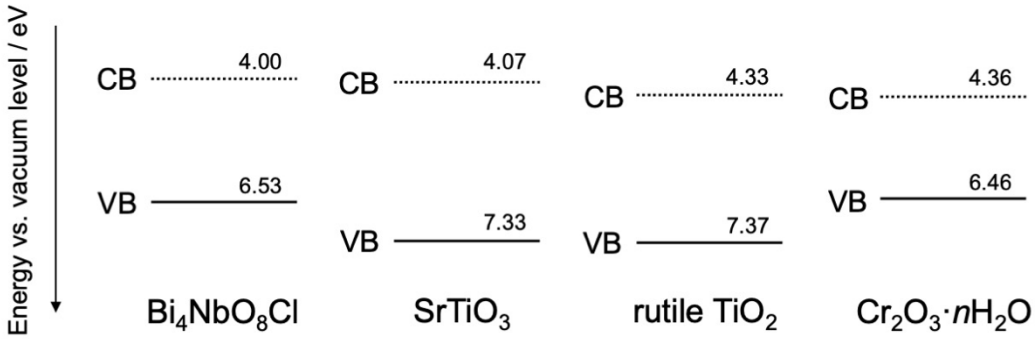

Figure S25. Energy level diagram for Bi_4NbO_8Cl, $SrTiO_3$, TiO_2, and $Cr_2O_3 \cdot nH_2O$.

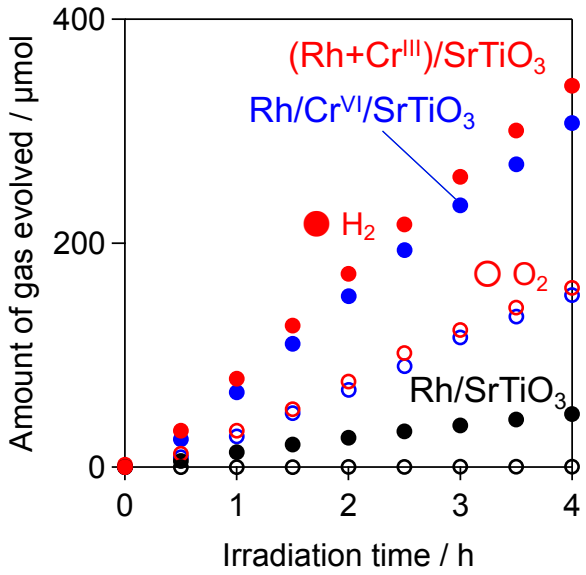

Figure S26. Time courses of overall water splitting of Rh and Cr loaded $SrTiO_3$. Every reaction was conducted with 0.1 g of the sample in pure water (250 mL) under UV irradiation ($\lambda > 300$ nm).

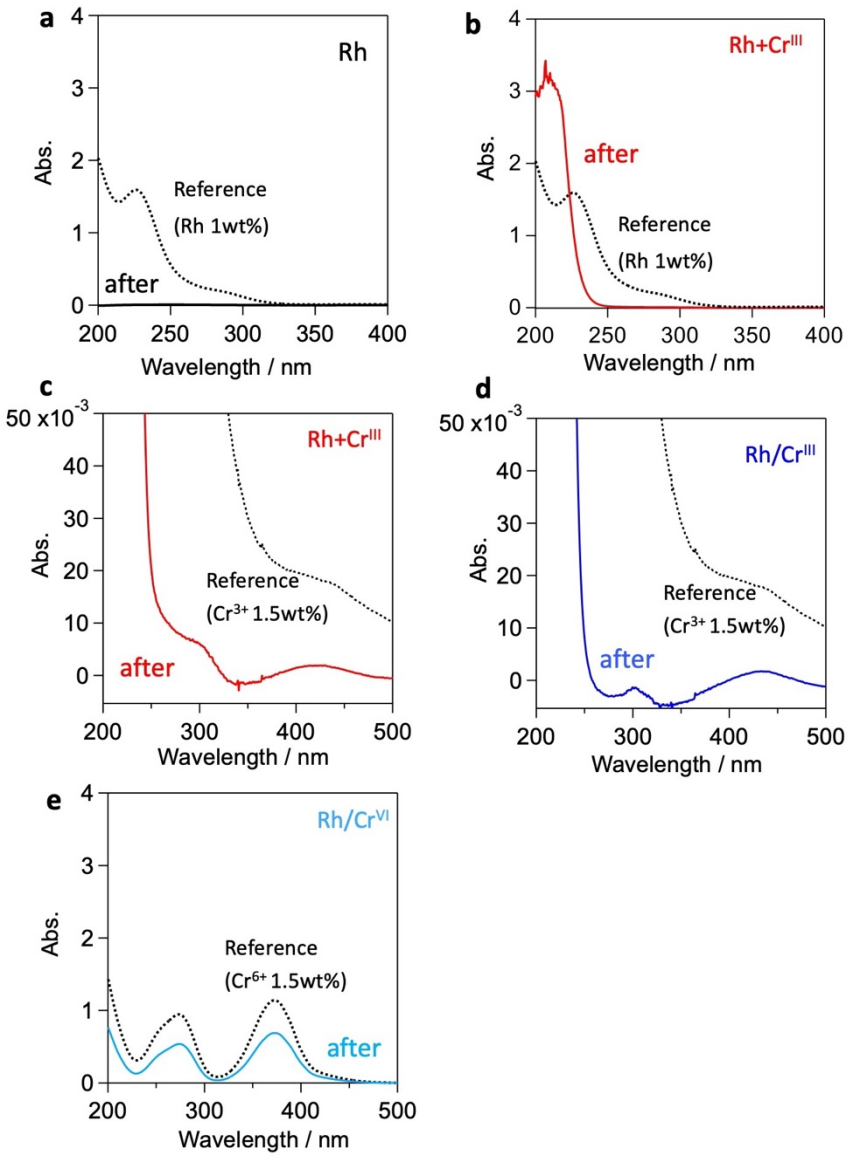

Figure S27. Absorption spectra of the solution after the PD process. Rh were fully consumed during the PD process for (a) Rh and (b) Rh+Cr^{III}, while the loading amount of Cr were approximately 1.3, 1.3, and 0.6 wt% for (c) Rh+Cr^{III}, and (d) Rh/Cr^{III}, (e) Rh/Cr^{VI} respectively.

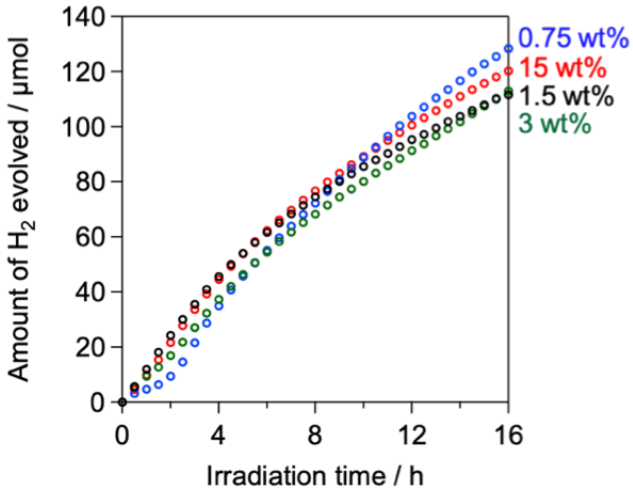

Figure S28. Time courses of H_2 evolution of H_2 evolution over Rh+Cr^{III} samples prepared with different concentration of Cr^{3+} precursor.